Journal of Solid State Chemistry **150,** 167–177 (2000)
doi:10.1006/jssc.1999.8573, available online at http://www.idealibrary.com on IDEAL®

New Calcium Tantalate Polytypes in the System $Ca_2Ta_2O_7$–$Sm_2Ti_2O_7$

Ian E. Grey* and Robert S. Roth†

*CSIRO Minerals, Bayview Avenue, Clayton, Victoria 3168, Australia; and †National Institute of Standards and Technology, Gaithersburg, Maryland 20899

Received June 24, 1999; accepted November 5, 1999

New calcium tantalate polytypes with weberite-related structures have been prepared by doping $Ca_2Ta_2O_7$ with $Sm_2Ti_2O_7$. Trigonal 6-layer (6T) and monoclinic 5-layer (5M) polytypes containing $\sim$6 and 10 mol%, respectively of the $Sm_2Ti_2O_7$ component were prepared and the structures were determined and refined using X-ray data on flux-grown single crystals. The 6T phase, $Ca_{1.89}Ta_{1.86}Sm_{0.16}Ti_{0.10}O_7$, has $a = 7.353(1)$, $c = 36.264(1)$ Å, $Z = 12$, space group $P3_1$, and the 5M phase, $Ca_{1.80}Ta_{1.80}Sm_{0.24}Ti_{0.17}O_7$, has $a = 12.763(1)$, $b = 7.310(1)$, $c = 30.190(1)$ Å, $\beta = 94.09°(1)$, $Z = 20$, space group $C2$. The 6T structure is related to the 3T weberite structure, having a cubic close packed metal atom array as in fluorite and a stacking of (001) metal atom layers ($\equiv\{111\}_f$) that alternately have the composition Ta_3Ca and Ca_3Ta. Hexagonal tungsten bronze type layers of corner-connected octahedra are interconnected by isolated TaO_6 octahedra in the Ca_3Ta layers, giving an octahedral framework of composition $[Ta_2O_7]^{4-}$ in which the eight-coordinated calcium atoms are distributed. The octahedra in the Ca_3Ta layers have only four anions involved in corner sharing. The different weberite polytypes are distinguished by the geometry of the two terminal anions, *cis*- or *trans*. In the 6T structure there is an alternation of *cis*- and *trans*- octahedra in successive Ca_3Ta layers. The 5M polytype differs from the weberite polytypes in having regular twinning of the metal atom lattice on (001), giving a stacking sequence *hccchccccc*.... The *c*-stacked blocks alternatively have the weberite and pyrochlore structures, with ordering of Sm into the Ca sites in the pyrochlore blocks.

INTRODUCTION

We have recently reported (1) preliminary results on new polytypes formed by $Ca_2Ta_2O_7$ using different conditions of preparation and different minor substitutions. Information on modes of substitution of impurity elements in calcium tantalate has potential applications to mineral processing. For example uran-microlite, $(Ca,Na,U)_2Ta_2(O,OH)_7$, is a significant component of tantalum mineral deposits and it causes problems in the production of commercial tantalite concentrates due to its uranium content (2, 3). Crystal chemistry knowledge concerning the mode of uranium incorporation could contribute to the selection of a processing route for its removal. Substituted $Ca_2Ta_2O_7$ phases are also of interest because of their dielectric properties which have potential applications in microwave communications devices (4).

Despite its compositional simplicity, a definitive structural characterisation has not been published for $Ca_2Ta_2O_7$. Low-temperature preparations have been reported to given the pyrochlore structure but the phase obtained was not stoichiometric (5). A solid-state preparation at 1200°C was reported to give a phase with hexagonal symmetry (6) but a structure analysis was not made. An inspection of the reported unit cell dimensions and powder pattern intensities indicates that at 1200°C, $Ca_2Ta_2O_7$ has the trigonal weberite, Na_2MnFeF_7, structure (7) which is a fluorite-derivative structure closely related to that for pyrochlore (8). On this basis the structure can be described in terms of cubic stacking of closest-packed cation layers ($\equiv\{111\}_{fluorite}$) where the layers alternately have the compositions Ta_3Ca and Ca_3Ta, as shown in Fig. 1. Oxygen coordination in the Ta_3Ca layers gives hexagonal tungsten bronze (HTB)-type motifs of corner-connected TaO_6 octahedra with CaO_8 hexagonal bipyramids occupying the hexagonal rings. The Ca_3Ta layers comprise strongly deformed CaO_8 cubes interconnected to each other and to isolated TaO_6 octahedra via edge sharing. The basic repeating unit is a 6-Å thick slab parallel to (001) comprising a Ca_3Ta layer and a Ta_3Ca layer. Three such blocks, stacked along [001] and offset relative to one another in accord with the symmetry of space group $P3_121$, complete the trigonal weberite structure for $Ca_2Ta_2O_7$. The shorthand notation for the three-block trigonal structure is 3T.

Using different preparation conditions and different minor substitutions we have prepared a number of calcium tantalate phases which have related X-ray diffraction patterns, comprising strong subcell reflections characteristic of the 6-Å basic structure motif, together with different distributions of superlattice reflections corresponding to the different stacking sequences of the 6-Å blocks (1). The diffraction patterns could all be indexed using trigonal or pseudotrigonal cells having $a \sim 7.3$ Å, $c \sim n \times 6$ Å, giving

0022-4596/00 $35.00

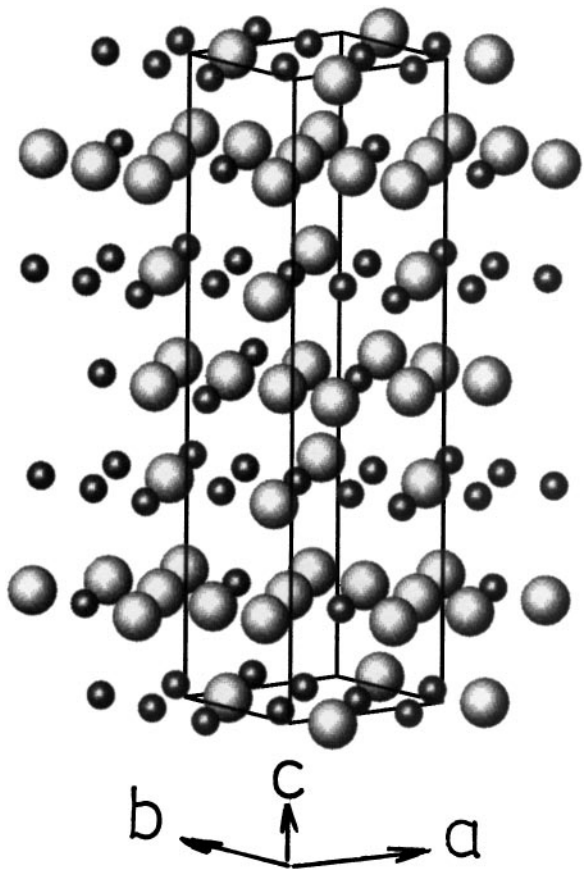

FIG. 1. Metal atom packing in the 3T weberite, $A_2B_2X_7$ structure. Large circles represent *A*, small circles represent *B*.

rise to a variety of polytypes such as 3T, 6T, 5M, 6M, 7M, (M = monoclinic, in which case $b \sim \sqrt{3}a$ or vice versa). We reported the structure determination of one of the pure (undoped) $Ca_2Ta_2O_7$ polytypes, 6M, using single-crystal X-ray data in conjunction with information from high-resolution TEM images. The structure analysis revealed another dimension to the complexity of the $Ca_2Ta_2O_7$ polytypes, not evident in any of the known weberite polytypes, due to periodic twinning of the cation array on (001) planes. In the case of the 6M polytype this gives a stacking sequence of cation layers of the type *cccchcccch*...

As part of a study of the effect of minor substitutions on the $Ca_2Ta_2O_7$ structure we carried out syntheses in the system $Ca_2Ta_2O_7$–$Sm_2Ti_2O_7$. Samarium titanate has the pyrochlore structure, which is one of the other main structure types (with weberite and zirconolite) adopted by $A_2B_2O_7$ compositions. Neither the inferred 3T structure nor the determined 6M structure for $Ca_3Ta_2O_7$ contain pyrochlore blocks and so it was interesting to determine if the substitution of a pyrochlore end-member would stabilize a $Ca_2Ta_2O_7$ polytype containing pyrochlore elements. Powder XRD patterns of polycrystalline products from heating experiments at 1650°C showed single-phase pyrochlore for compositions containing greater than 40 mol % $Sm_2Ti_2O_7$ and gave weberite-related polytype patterns at less than 20 mol % $Sm_2Ti_2O_7$. A crystal growth experiment using a 10 mol % $Sm_2Ti_2O_7$ charge in Sm-doped calcium vanadate as flux gave a product displaying a relatively simple weberite-type powder XRD pattern with superlattice reflections lying halfway between those for 3T $Ca_2Ta_2O_7$ (6). The pattern could be indexed on the basis of a 6T polytype.

However, diffraction studies on individual single crystals showed that in addition to the 6T phase the reaction product contained crystals of a 5M polytype. Microprobe analyses on the two types of crystals showed different levels of incorporated Sm and Ti, suggesting that the minor substitutions were influencing the polytype stacking. Structure determinations were carried out on both polytypes, the results of which are reported here together with a comparsion of the crystal chemistry of these and other polytypes.

EXPERIMENTAL

Crystal Growth

For the crystal growth experiment a mixture of AR grade $CaCO_3$, Ta_2O_5, Sm_2O_3, and TiO_2 corresponding to the composition $(Ca_2Ta_2O_7)_{0.9}(Sm_2Ti_2O_7)_{0.1}$ was finely ground and heated to 900°C to decompose the carbonate. It was then combined with a flux of composition $Ca_{1.8}Sm_{0.2}V_2O_7$ in the weight ratio 50 : 50 and the mixture was sealed in a platinum tube. The sample was heated to 1550°C, held for 24 h then cooled to 1200°C at 2°C/h. The sample was held at this temperature for 16 h and then removed from the furnace. The excess flux was dissolved in hot dilute HCl plus methanol. The product was in the form of dense aggregates of anhedral crystals that had to be separated by crushing the aggregates. Breakage gave parting of the aggregates along a preferred direction, resulting in irregular-shaped, platy crystals, with the trigonal or pseudotrigonal *c*-axis within the plane of the plate. This contrasts with crystal growth experiments on undoped $Ca_2Ta_2O_7$, which gave hexagonal platelets (1).

Analyses

Wavelength-dispersive electron microprobe analyses were obtained on crystals of the 6T and 5M polytypes, using a JEOL Superprobe microanalyser model JXA-8900R, operated at 20 kV and 30 nA. Standards used were synthetic $Ca_2Ta_2O_7$, Sm metal, V metal, and TiO_2. The results of points analyzed in different regions of the crystals are reported in Table 1. They show a high compositional homogeneity within the crystals. A trace amount of vanadium is present, incorporated from the flux, the amount being

TABLE 1
Microprobe Analyses (wt%, Expressed as Oxides) for 5M and 6T Crystals

	6T analyses			5M analyses		
	1	2	3	1	2	3
CaO	19.0	18.9	18.9	18.1	18.5	18.2
Ta_2O_5	74.8	74.8	74.6	72.0	72.0	71.7
Sm_2O_3	5.1	5.0	5.2	7.4	7.2	7.6
TiO_2	1.3	1.4	1.5	2.3	2.2	2.4
V_2O_5	0.0	0.1	0.1	0.4	0.2	0.4
Total	100.2	100.2	100.3	100.2	100.1	100.3

higher for the 5M crystal. Formulas derived from the microprobe analyses (V grouped with Ti) are given in Table 2.

Single Crystal Structure Studies

Crystals from the flux growth experiment were first checked using the precession method. Individual crystals were found to be single phase, corresponding to one or other of two different polytypes, having either trigonal symmetry with $c \sim 36$ Å $\equiv$ 6T, or monoclinic *C*-centered symmetry with $c \sim 30$ Å $\equiv$ 5M. The only systematic reflection extinctions observed in the precession photos of the 6T polytype were for 00*l*, $l \neq 3n$. The 5M diffraction patterns showed reflection absences due only to the *C*-centering, giving possible space groups of *C*2/*m*, *Cm*, or *C*2.

TABLE 2
Summary of Data Collection Conditions and Refinement Parameters

	5M polytype	6T polytype
Formula (microprobe)	$Ca_{1.80}Ta_{1.80}Sm_{0.24}Ti_{0.17}O_7$	$Ca_{1.89}Ta_{1.86}Sm_{0.16}Ti_{0.10}O_7$
Crystal data		
Cell parameters	$a = 12.763(1)$, $b = 7.310(1)$ $c = 30.190(1)$ Å, $\beta = 94.09°(1)$	$a = 7.353(1)$ $c = 36.264(1)$ Å
Z	20	12
Space group	*C*2	$P3_1$
Intensity measurements		
Temperature (K)	150	293
λ (Mo$K\alpha$)	0.71073	0.71073
Crystal size, mm	$0.025 \times 0.075 \times 0.11$	$0.035 \times 0.040 \times 0.050$
Collection mode	ϕ scan, 0–360° 720 frames at $\Delta\phi = 0.5°$	as for 5M
Count time per frame	30 s	70 s
Crystal-to-detector	35 mm	40 mm
θ-offset (°)	0	0
2θ max. (°)	50	42
Total no. reflections	11,612	14,695
No. unique reflections	4,444	3,164
No. reflections, $F > 4\sigma(F)$	4095	2660
Absorption correction	Empirical, $\mu = 39.1$ mm^{-1}	$\mu = 39.3$ mm^{-1}
A_{min}, A_{max}	0.21, 0.76	0.39, 0.45
R(merge) on F^2	0.06	0.06
Refinement		
Parameters refined	239	193
w$R2$ ($F2$), all data	0.11	0.09
$R1$, $F > 4\sigma(F)$	0.042	0.038
$R1$, all data	0.049	0.051
Max peak in ΔF map, e/Å^3	3.0	1.4

Single crystal intensity data collections were made using a Nonius Kappa diffractometer employing a CCD area detector. The data collection conditions for both polytypes are given in Table 2. To minimize possible effects of absorption, the crystals used for the data collection were dissected to reduce the average dimensions to ~ 50 μm. The CCD intensity data sets were processed to produce absorption-corrected data files of F^2 and $\sigma(F^2)$, which were used with SHELXL (9) for the structure determination and refinements.

5M structure. The structural principles established for the 6M polytype (1) were used to develop a starting structure model for the 5M polytype. The metal–metal vectors in the 3D Patterson map were used to establish the stacking sequence of (001) metal atom layers as *ccchccccch*.... By analogy with the 6M structure, the layer compositions were made alternately Ca_3Ta and Ta_3Ca, and the *h*-stacked layers were assigned as Ta_3Ca. The intralayer ordering of Ca and Ta was determined by exhaustive testing of all possible combinations using the low-angle single-crystal intensity data. A satisfactory model could only be established using the space group *C*2. Refinement of the best metal atom arrangement obtained using this space group gave an agreement factor $R1 = 0.16$. The positions of the oxygen atoms were located in successive difference Fourier maps.

Refinement of atomic positions and isotropic displacement parameters gave $R1 = 0.12$ for all data. Some of the calcium sites had large negative displacement parameters and high electron residuals in difference Fourier maps, strongly suggesting the ordering of samarium atoms at these sites. Similarly some tantalum sites had elevated displacement parameters corresponding to titanium substitution. The refinement was continued with allowance for Sm/Ca and Ta/Ti substitutions, resulting in final convergence at the R values given in Table 2. The calculated composition based on the refined site occupation factors (SOF) is $Ca_{1.75}Ta_{1.84}Sm_{0.25}Ti_{0.16}O_7$, in good agreement (within 2 e.s.d's of the refined SOF's) with the composition obtained from the microprobe analyses in Table 2. The refined atomic coordinates and isotropic displacement parameters are given in Table 3. The refined SOF's for the metal atom sites are given in Table 4. A table of structure factors is available from the authors.

6T structure. The observed systematic extinction for reflections 00*l*, $l \neq 3n$, indicated that possible trigonal space groups were $P3_1$, $P3_121$, and $P3_112$ (and their enantiomorphic forms). $P3_121$ was selected on the basis of the observed

TABLE 3
Atomic Coordinates ($\times 10^4$) and Equivalent Isotropic Displacement Parameters (Å$^2 \times 10^3$) for the 5M Polytype

Atom	x	y	z	U (eq)
Ta(1)	0	85	0	3(1)
Ca(11)	0	5162(5)	0	4(1)
Ca(12)	2502(2)	2641(6)	−2(1)	4(1)
Ta(2)	1845(1)	20(4)	1008(1)	5(1)
Ca(21)	1830(1)	5006(6)	991(1)	4(1)
Ta(22)	4328(1)	2489(3)	996(1)	4(1)
Ta(23)	4330(1)	7500(3)	998(1)	6(1)
Ta(3)	3732(1)	−8(3)	2025(1)	6(1)
Ca(31)	3624(2)	4971(8)	1984(1)	8(1)
Ca(32)	6206(3)	2434(8)	1974(1)	9(1)
Ca(33)	6210(3)	7470(8)	1994(1)	10(1)
Ca(4)	5521(3)	−47(11)	2992(1)	8(1)
Ta(41)	5564(1)	5036(3)	2945(1)	5(1)
Ta(42)	8072(1)	2507(3)	3039(1)	5(1)
Ta(43)	8051(1)	7526(3)	3020(1)	5(1)
Ca(5)	4036(3)	64(9)	3992(1)	7(1)
Ca(51)	3957(4)	4958(11)	4066(1)	18(1)
Ca(52)	6539(3)	2527(8)	4015(1)	10(2)
Ta(53)	6384(1)	7542(3)	3983(1)	4(1)
Ta(6)	2506(1)	9991(3)	4979(1)	6(1)
Ta(61)	5000	2489(4)	5000(1)	6(1)
Ca(62)	5000	7644(11)	5000	7(2)
O(1)	3283(9)	12(24)	9753(4)	5(2)
O(2)	4413(12)	6984(18)	358(4)	9(3)
O(3)	4398(12)	3024(20)	349(5)	13(4)
O(4)	6337(9)	5024(24)	359(5)	10(3)
O(5)	4767(9)	75(23)	842(4)	6(2)
O(6)	2811(11)	8050(17)	863(4)	0(3)
O(7)	7837(12)	6946(18)	839(4)	6(3)
O(8)	3895(9)	5068(23)	1125(4)	6(2)
O(9)	5821(11)	6928(18)	1137(4)	5(3)
O(10)	5874(12)	3017(19)	1138(5)	8(3)
O(11)	4215(11)	8002(18)	1627(4)	8(3)
O(12)	7319(9)	5039(24)	1638(4)	11(3)
O(13)	4205(11)	1993(17)	1615(4)	6(3)
O(14)	6956(9)	9963(24)	1719(4)	8(2)
O(15)	5137(9)	60(25)	2278(4)	6(2)
O(16)	332(9)	−30(26)	2312(4)	8(3)
O(17)	3076(11)	8083(17)	2347(4)	2(3)
O(18)	3217(12)	2046(19)	2362(5)	11(3)
O(29)	2730(9)	5065(23)	2840(4)	10(3)
O(20)	1551(10)	2027(16)	2849(4)	0(3)
O(21)	1574(13)	7975(22)	2963(5)	20(4)
O(22)	4547(10)	7004(17)	3007(4)	0(3)
O(23)	4537(13)	3324(21)	3133(5)	17(3)
O(24)	3526(10)	80(26)	3139(4)	16(3)
O(25)	2817(10)	2774(20)	3642(4)	8(3)
O(26)	995(11)	386(19)	3612(4)	16(3)
O(27)	8102(11)	2262(21)	3673(4)	13(3)
O(28)	810(10)	4679(18)	3702(4)	9(3)
O(39)	128(10)	2299(21)	4280(4)	9(3)
O(30)	22(11)	7437(24)	4343(4)	15(3)
O(31)	7208(12)	5506(19)	4354(5)	18(4)
O(32)	2189(12)	4275(19)	4388(5)	13(3)
O(33)	986(9)	5372(17)	5093(4)	0(3)
O(34)	8984(13)	9488(20)	4926(5)	19(4)
O(35)	2260(10)	2378(19)	5215(4)	8(3)

Laue symmetry ($R_{merge} = 0.062$). The metal–metal vectors in the Patterson map were consistent with a cubic stacking of metal atom layers. Metal atom ordering models were constrained to comprise alternating (001) layers of composition Ca_3Ta and Ta_3Ca as in the 5M and 6M polytypes. Screening of different intralayer Ca/Ta ordering models was made using the Rietveld method in conjunction with the experimental powder pattern. This enabled a rapid visual check of a large number of possible models. This procedure is well suited to phases such as tantalates, where the intensities of the diffraction peaks are determined predominantly by the metal atom contributions.

The metal atom model giving the best fit to the powder XRD data was refined using the single crystal data, giving $R_1 = 0.13$. The oxygen atoms were located in difference Fourier maps. Refinement of all atom coordinates and isotropic displacement parameters converged at $R_1 = 0.07$. The refined displacement parameters for a number of oxygen atoms were higher than normal for a dense structure ($U \sim 0.03$–0.05), and so the possibility of a lowering of the symmetry to $P3_1$ was examined. The metal atom ordering from the $P3_121$ refinement was maintained. The structure refined smoothly in $P3_1$ to $R_1 = 0.05$ for all reflections. The resulting isotropic displacement parameters for the oxygen atoms decreased to more reasonable values (range of $U = 0.004$–0.017) and the heights of residual peaks in the

TABLE 4
Refined Metal Atom Site Occupancies in the 5M Polytypes

Site	Occupancy
Ta(1)	0.434(3) Ta + 0.066 Ti
Ca(11)	0.330(5) Ca + 0.170 Sm
Ca(12)	0.681(8) Ca + 0.319 Sm
Ta(2)	0.866(7) Ta + 0.133 Ti
Ca(21)	0.666(9) Ca + 0.334 Sm
Ta(22)	0.806(8) Ta + 0.194 Ti
Ta(23)	0.833(7) Ta + 0.167 Ti
Ta(3)	Ta
Ca(31)	0.900(9) Ca + 0.100 Sm
Ca(32)	0.904(9) Ca + 0.096 Sm
Ca(33)	0.885(9) Ca + 0.115 Sm
Ca(4)	Ca
Ta(41)	0.982(8) Ta + 0.078 Ti
Ta(42)	0.960(7) Ta + 0.040 Ti
Ta(43)	0.937(9) Ta + 0.063 Ti
Ca(5)	Ca
Ca(51)	Ca
Ca(52)	0.903(9) Ca + 0.097 Sm
Ta(53)	0.945(9) Ta + 0.055 Ti
Ta(6)	0.948(8) Ta + 0.052 Ti
Ta(61)	0.487(5) Ta + 0.013 Ti
Ca(62)	0.465(6) Ca + 0.035 Sm

TABLE 5
Atomic Coordinates ($\times 10^4$) and Equivalent Isotropic Displacement Parameters ($Å^2 \times 10^3$) for the 6T Polytype

	x	*y*	*z*	*U* (eq)
Ca(1)	1812(8)	1813(8)	−36(1)	9(1)
Ta(11)	6676(3)	6679(2)	10(1)	3(1)
Ca(12)	1771(9)	6797(9)	−18(2)	9(1)
Ca(13)	6685(9)	1762(7)	−30(2)	14(1)
Ca(2)	−36(13)	8371(12)	9202(3)	17(3)
Ta(21)	132(2)	3477(2)	9173(1)	5(1)
Ta(22)	5113(3)	8470(2)	9174(1)	10(1)
Ta(23)	5106(2)	3436(3)	9147(1)	7(1)
Ta(3)	3167(2)	−169(2)	8344(1)	3(1)
Ca(31)	8569(9)	341(9)	8364(2)	12(2)
Ca(32)	3648(7)	5207(7)	8303(2)	6(1)
Ca(33)	8569(8)	5207(9)	8327(2)	6(1)
Ta(4)	1796(3)	1759(3)	7507(1)	9(1)
Ta(41)	6820(2)	6801(2)	7510(1)	3(1)
Ca(42)	1750(11)	6635(12)	7480(2)	16(3)
Ta(43)	6768(3)	1755(3)	7537(1)	7(1)
O(1)	585(27)	8723(25)	8602(5)	15(5)
O(2)	4593(27)	2687(28)	8639(5)	18(5)
O(3)	9525(24)	8171(20)	9801(5)	9(4)
O(4)	3783(23)	5327(20)	207(4)	7(3)
O(5)	1588(22)	2359(23)	6995(4)	17(4)
O(6)	6040(26)	1289(23)	8064(4)	6(4)
O(7)	4749(24)	8867(23)	8646(4)	9(4)
O(8)	2021(24)	7251(26)	8085(5)	12(4)
O(9)	9742(26)	3267(20)	9732(7)	19(6)
O(10)	7630(20)	5229(19)	331(4)	9(4)
O(11)	5698(21)	8266(20)	9691(4)	11(3)
O(12)	2168(21)	1421(23)	8044(4)	4(4)
O(13)	7032(23)	7235(28)	8054(5)	18(4)
O(14)	8079(21)	4463(21)	9078(4)	12(3)
O(15)	7807(21)	4766(21)	7601(4)	11(3)
O(16)	5763(21)	8777(19)	7430(4)	10(3)
O(17)	2133(19)	2474(20)	9260(4)	7(3)
O(18)	6644(17)	6454(21)	6983(6)	6(5)
O(19)	9878(18)	8799(19)	7422(4)	10(3)
O(20)	5716(20)	4293(21)	9679(4)	11(3)
O(21)	9594(17)	2377(21)	7674(4)	14(3)
O(22)	4519(20	658(18)	9324(4)	14(3)
O(23)	5677(20)	6283(17)	9014(4)	11(3)
O(24)	4024(18)	1210(19)	7368(3)	10(3)
O(25)	8109(20)	468(19)	9081(4)	8(3)
O(26)	3813(19)	4815(21)	7600(4)	8(3)
O(27)	2166(20)	6531(19)	9259(4)	12(3)
O(28)	537(24)	3690(20)	8631(5)	5(4)

difference Fourier map were halved. The refinement parameters for the $P3_1$ refinement are given in Table 2. The refined atomic coordinates and isotropic displacement parameters are reported in Table 5. In contrast to the refinement of the 5M polytype, the refinement of the 6T polytype showed no significant ordering of Sm and Ti into specific Ca and Ta sites.

RESULTS AND DISCUSSION

The 6T Phase

A projection of the structure of the 6T $Ca_2Ta_2O_7$ polytype along [110] is shown in Fig. 2. The structure represents a new variation of the weberite structure closely related to the 3T polytype. To a good approximation the 6T structure can be described in the same space group, $P3_121$, as the 3T structure and can be derived from it by a doubling of the *c*-axis and an interchange of a calcium and a tantalum atom in one of the (001) $CaTa_3$ layers (and in the symmetry related layers).

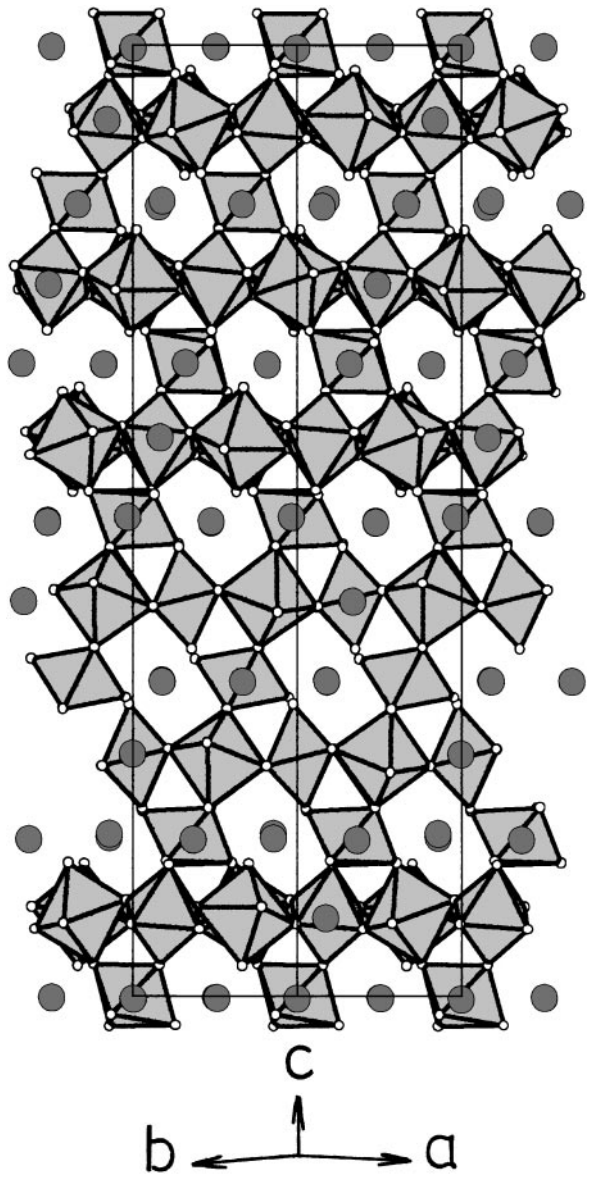

FIG. 2. Polyhedral representation of the structure of the 6T $Ca_2Ta_2O_7$ polytype viewed along the [110] direction. Large circles represent calcium atoms.

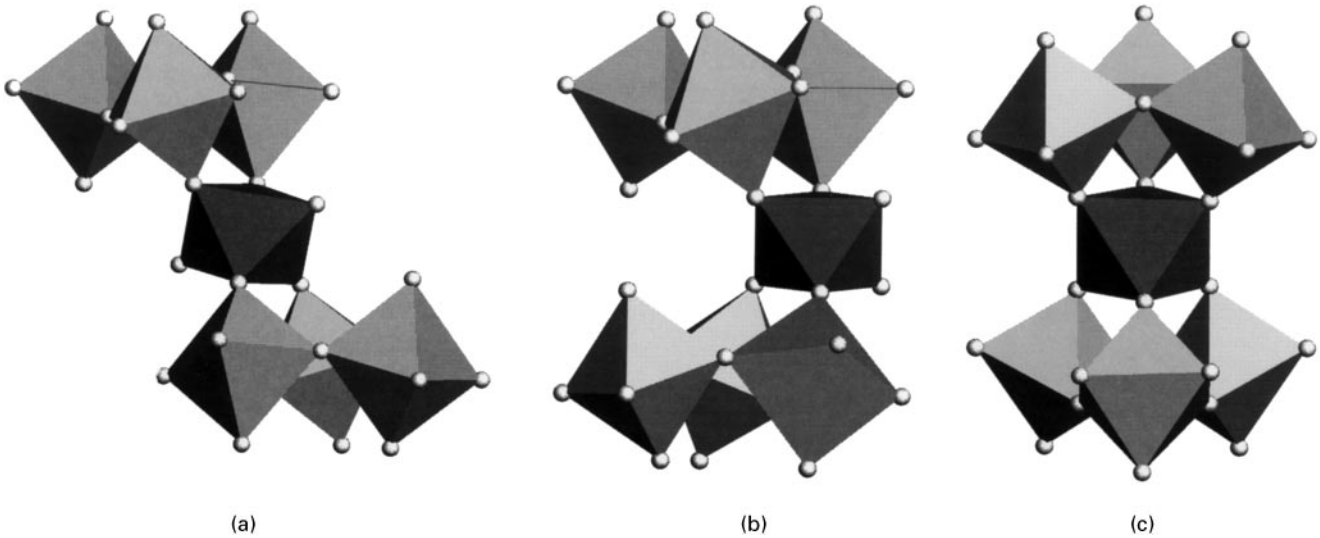

FIG. 3. Octahedral connectivity in $A_2B_2X_7$ structures between the triangular groupings of corner-shared octahedra in pairs of HTB layers via the isolated octahedra in the A_3B layers. (a) *trans*-configuration of the linking octahedron in weberite, (b) *cis*-configuration in weberites, (c) connectivity in pyrochlore.

In Fig. 2, the TaO_6 octahedra are shown in polyhedral form. Corner-linking of the octahedra in the Ta_3Ca layers gives hexagonal tungsten bronze (HTB) layers with Ca atoms located at the centers of the hexagonal rings in hexagonal bipyramidal coordination. The intervening layers of composition Ca_3Ta (large-cation layers) have a complementary arrangement of metal atoms to that in the Ta_3Ca layers, with hexagonal rings of Ca atoms and Ta atoms in the centres of the rings. The Ca atoms are in distorted cubic coordination and are interconnected within the layer to each other and to the TaO_6 octahedra by edge sharing. The isolated TaO_6 octahedra in the Ca_3Ta layers are oriented so that one of the octahedral three-fold axes is parallel to [001]. These octahedra share corners with pairs of octahedra from the HTB layers on either side. The remaining two vertices of the octahedra in the Ca_3Ta layers are terminal.

The various weberite polytypes are distinguished by the relative positions of the terminal anions in the isolated octahedra in the large-cation layers. These are in a *cis*-configuration in 3T weberite and in a *trans*-configuration in the orthorhombic form (8). These are illustrated in Fig. 3. The 4M weberite polytype has an alternation of *cis*- and *trans*- forms in successive large-cation layers (8). The 6T polytype of $Ca_2Ta_2O_7$ also has an alternation of *cis*- and *trans*- configurations for TaO_6 in successive Ca_3Ta layers, as illustrated in Fig. 4. Whereas in the 4M polytype only two of the three possible *trans*-configurations occurs, all three are found in the 6T polytype.

Average polyhedral M–O bond lengths, together with upper and lower values for the 6T structure are given in Table 6. The Ta–O and Ca–O distances lie in the ranges 1.90 to 2.11 Å and 2.19 to 2.99 Å, respectively. The average distances are within relatively tight ranges, 1.95 to 2.00 Å for ⟨Ta–O⟩ and 2.55 to 2.62 Å for ⟨Ca–O⟩. The ⟨Ta–O⟩ are generally shorter and the ⟨Ca–O⟩ longer than expected on

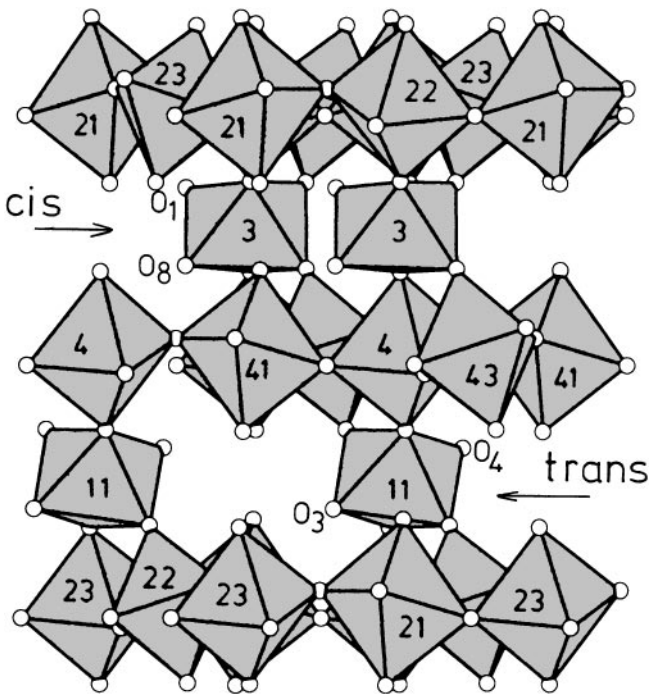

FIG. 4. Part of the 6T octahedral framework, rotated 30° about c^* from the projection in Fig. 2. The terminal oxygen atoms associated with *cis*- and *trans*-TaO_6 in the Ca_3Ta layers are labeled, as are the tantalum atoms.

TABLE 6
***M*–O and *M*–*M* Polyhedral Distances (Å) for the 5M and 6T Tantalate Polytypes**

Site	CN	⟨*M*–O⟩	Range	Layer type	*M* polyhedr.	⟨*M*–*M*⟩	Range
				5M			
Ta(1)	6	1.97	1.94–2.02	pyCa_3Ta	6Ta + 6Ca	3.68	3.60–3.71
Ta(2)	6	1.98	1.95–2.01	pyTa_3Ca	”	3.67	3.61–3.76
Ta(22)	6	1.97	1.92–2.03	”	”	3.67	3.65–3.72
Ta(23)	6	1.97	1.91–2.03	”	”	3.68	3.64–3.73
Ta(3)	6	1.98	1.90–2.08	pyCa_3Ta	5Ta + 7Ca	3.68	3.57–3.79
Ta(41)	6	1.97	1.91–2.07	*h*-Ta_3Ca	”	3.71	3.51–**4.07**
Ta(42)	6	1.97	1.92–2.13	”	”	3.69	3.57–3.85
Ta(43)	6	1.97	1.91–2.04	”	6Ta + 6Ca	3.68	3.58–3.74
Ta(53)	6	2.01	1.90–2.17	*cis* Ca_3Ta	4Ta + 8Ca	3.68	3.52–3.84
Ta(6)	6	1.97	1.92–2.03	w-Ta_3Ca	6Ta + 6Ca	3.67	3.54–3.79
Ta(61)	6	1.98	1.96–2.00	w-Ta_3Ca	4Ta + 8Ca	3.64	3.52–3.76
Ca(11)	8	2.51	2.27–2.69	pyCa_3Ta	6Ta + 6Ca	3.67	3.60–3.73
Ca(12)	8	2.52	2.16–2.70	”	”	3.67	3.60–3.73
Ca(21)	8	2.52	2.19–2.64	pyTa_3Ca	”	3.66	3.59–3.70
Ca(31)	8	2.55	2.22–2.90	pyCa_3Ta	7Ta + 5Ca	3.68	3.57–3.79
Ca(32)	8	2.57	2.21–3.02	”	6Ta + 6Ca	3.67	3.57–3.85
Ca(33)	8	2.55	2.24–2.74	”	”	3.66	3.52–3.77
Ca(4)	8	2.54	2.16–2.89	*h*-Ta_3Ca	8Ta + 4Ca	3.67	3.57–3.76
Ca(5)	8	2.59	2.35–2.77	*cis* Ca_3Ta	6Ta + 6Ca	3.65	3.52–3.84
Ca(51)	7	2.53	2.29–3.04	”	7Ta + 5Ca	3.69	3.52–**4.07**
Ca(52)	7	2.49	2.24–2.73	”	”	3.68	3.56–3.84
Ca(62)	8	2.53	2.21–2.92	w-Ta_3Ca	8Ta + 4Ca	3.65	3.54–3.77
				6T			
Ta(11)	6	1.97	1.93–2.01	*trans* Ca_3Ta	4Ta + 8Ca	3.68	3.58–3.78
Ta(21)	6	2.00	1.97–2.04	w-Ta_3Ca	”	3.67	3.55–3.87
Ta(22)	6	1.95	1.93–1.98	”	6Ta + 6Ca	3.67	3.57–3.78
Ta(23)	6	1.96	1.90–2.01	”	”	3.68	3.61–3.76
Ta(3)	6	1.99	1.90–2.11	*cis* Ca_3Ta	4Ta + 8Ca	3.69	**3.39–3.96**
Ta(4)	6	1.97	1.93–2.01	w-Ta_3Ca	6Ta + 6Ca	3.71	3.60–**3.91**
Ta(41)	6	1.98	1.92–2.00	”	4Ta + 8Ca	3.70	3.51–3.87
Ta(43)	6	1.97	1.95–2.03	”	6Ta + 6Ca	3.71	3.61–**3.93**
Ca(1)	8	2.62	2.41–2.99	*trans* Ca_3Ta	6Ta + 6Ca	3.68	3.53–**3.91**
Ca(12)	8	2.61	2.37–2.95	”	”	3.68	3.56–**3.93**
Ca(13)	8	2.56	2.13–2.97	”	8Ta + 4Ca	3.70	3.57–3.87
Ca(2)	8	2.56	2.19–2.93	w-Ta_3Ca	”	3.66	3.53–3.76
Ca(31)	8	2.55	2.27–2.82	*cis* Ca_3Ta	7Ta + 5Ca	3.69	3.55–3.83
Ca(32)	8	2.56	2.31–2.89	”	”	3.69	3.51–3.87
Ca(33)	8	2.59	2.38–2.80	”	6Ta + 6Ca	3.68	**3.39–3.96**
Ca(42)	8	2.55	2.21–2.94	w-Ta_3Ca	8Ta + 4Ca	3.68	3.60–3.75

the basis of the ionic radii (10), and calculation of metal atom valences using the empirical parameters of Brese and O'Keeffe (11) gives elevated valences for Ta (up to 5.5) and depressed valences for Ca (down to 1.6). Thus in $Ca_2Ta_2O_7$ the Ta–O bonds are in relative compression while the Ca–O bonds are under tension.

The largest polyhedral distortion in the 6T structure is associated with the *cis*-Ta(3)O_6 octahedron, shown in Fig. 4, and involves a displacement of the tantalum atom toward the edge comprising the two terminal oxygens, O(1) and O(8). The displacement of Ti(3) is toward Ca(33) and as seen from Table 6, gives rise to alternating short and long *M*–*M* distances, 3.39 and 3.96 Å, respectively, along Ta(3)–Ca(33) chains in the Ca_3Ta layer. An inspection of published structure data for weberite polytypes (8) shows that a strong perturbation to the metal atom array associated with the *cis* octahedra is a consistent feature of these structures, and it results in a macroscopic elongation of the structure in the direction of the chains. The strong polarization of the Ta–O bonds associated with the large Ta displacements may be at the origin of the measured high dielectric constant for $Ca_2Ta_2O_7$ (4).

From Table 6 it is seen that the other major perturbations to the close-packed metal atom array involve distances between the calcium atoms Ca(1)–Ca(13) in the Ca_3Ta layer at $z = 0$ (containing the *trans*-Ta(11)O_6 octahedron) and the

tantalum atoms Ta(4)–Ta(43) in the adjacent Ta_3Ca layer at $z = \frac{1}{12}$. Predominantly vertical displacements of the atoms lead to Ca–Ta distances that are ~ 0.2 Å longer than the mean M–M (3.68 Å) distance. There is a corresponding but smaller shortening of Ca–Ta distances to tantalum atoms in the Ta_3Ca layer at $z = -\frac{1}{12}$. The longer Ca–Ta distances associated with the *trans*-Ca_3Ta layer results in a macroscopic expansion of the structure perpendicular to the metal atom layers which is manifested in the unit-cell parameters.

The 6T form of $Ca_2Ta_2O_7$ contains 1.9 atoms of Sm and 1.2 atoms of Ti per unit cell. No clear evidence for ordering of Sm and/or Ti could be obtained from the structure refinement. Nevertheless, the incorporation of these elements is necessary to stabilize the 6T polytype. In the absence of doping elements, $Ca_2Ta_2O_7$ forms the 3T polytype at temperatures below 1450°C and a 7M polytype at higher temperatures (1). In this study we have found that heating of $Ca_2Ta_2O_7$ doped with 10 mol % of $Sm_2Ti_2O_7$ also gives the 3T form at 1450°C, whereas the 6T polytype formed at 1650°C. A composition containing 30 mol % $Sm_2Ti_2O_7$ formed a mixture of 3T and pyrochlore at 1450°C and gave a mixture of 6T and pyrochlore at 1650°C. A 50 : 50 mol % composition gave pyrochlore at both temperatures.

The composition of the 6T polytype $Ca_{1.89}Ta_{1.86}Sm_{0.16}Ti_{0.10}O_7$ contains more samarium than is required to substitute for calcium in the A sites, and so some samarium substitution for tantalum must also occur. The partial replacement of Ta^{5+} by the larger Sm^{3+} is consistent with the unit-cell volume per formula unit for the 6T polytype, 141.5 Å, being slightly larger than those for the undoped $Ca_2Ta_2O_7$ polytypes, 141.2 Å^3 (1), despite Sm^{3+} and Ti^{4+} being smaller than Ca^{2+} and Ta^{5+}, respectively. Inspection of the bond lengths in Table 6 shows that Ta(21) has the longest mean Ta–O bond length of 2.00 Å, and that the longer bonds cannot be explained by distortion because the range of Ta(21)–O bonds, 0.07 Å, is smaller than in the mean range, 0.095 Å. Thus the samarium most likely substitutes at this site, which is a *trans*- octahedral site in the Ta_3Ca layer $z = -\frac{1}{12}$. Ta(21)O_6 octahedra link together chains of Ta(22)O_6 and Ta(23)O_6 within the Ta_3Ca layer as shown in Fig. 4 so the terminal *trans* vertices are above and below the Ca_3Ta plane. The chemical distinction between the Ta_3Ca layers at $z = 1/12$ and $-\frac{1}{12}$, due to ordering of samarium in the layer at $z = -\frac{1}{12}$ may be the basis for the asymmetrical interlayer M–M separations between metals in these layers and the intervening *trans*-Ca_3Ta layer, and ultimately this may be the cause for the particular stacking sequence adopted by the 6T polytype. It would be of interest to refine the structure of the 3T samarium titanate-doped structure that forms at temperatures lower than the 6T polytype in order to check if a different distribution of dopant elements occurs. To date we have not been successful in producing single crystals of the samarium titanate-doped 3T polytype.

The 5M Phase

A view of th 5M structure along [010] is shown in Fig. 5. In common with other tantalate polytypes (1), alternating (001) metal atom layers of composition Ca_3Ta and Ta_3Ca stack along the c direction. In contrast to the 6T and 3T structures, which have c stacking of the layers, the 5M structure has a mixture of cubic and hexagonal stacking of the layers according to the sequence *hccchccccch*. The *h*-stacked layers are HTB layers (Ta_3Ca) as found also for the 6M polytype with stacking sequence *hccccchccccch*. . . (1). However, whereas in the 6M structure the *c*-stacked blocks are of weberite-type, in the 5M structure blocks of weberite-type alternate with blocks of pyrochlore-type. The pyrochlore and weberite blocks are delineated in Fig. 5. The Sm is preferentially ordered in Ca sites in the pyrochlore blocks, Ca(11), Ca(12), and Ca(21). As seen from Table 4, two-thirds of the Sm occurs in these three sites, giving more than 30% occupancy by Sm, whereas the other eight Ca sites contain 10% or less of Sm.

The partial replacement of the weberite structure by a pyrochlore block in $Ca_2Ta_2O_7$ by doping with $Sm_2Ti_2O_7$ is

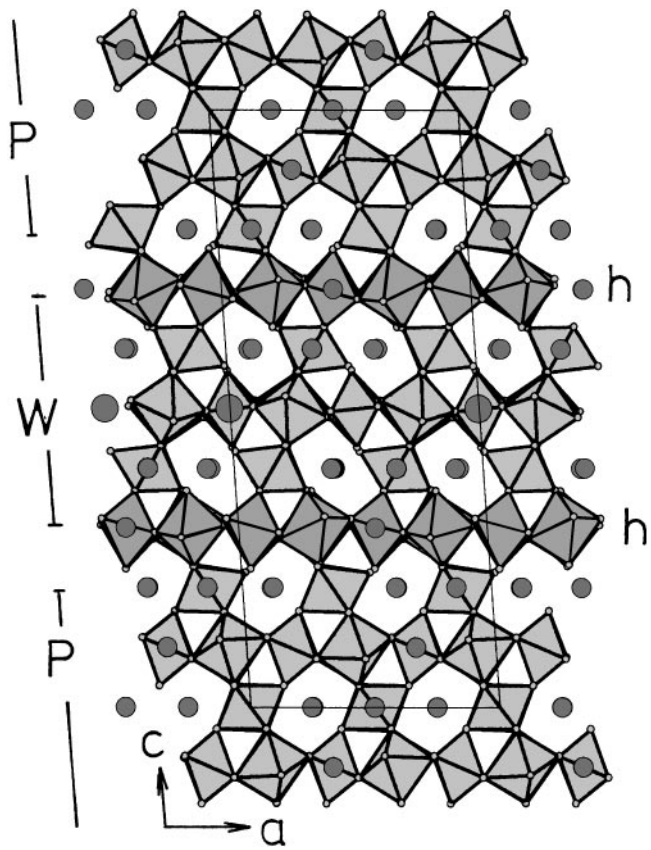

FIG. 5. Polyhedral representation of the structure of the 5M $Ca_2Ta_2O_7$ polytype viewed along the [010] direction. Large circles represent calcium atoms. The weberite (W) and pyrochlore (P) blocks are identified. The *h*-stacked HTB layer of octahedra is shown in dark shading.

consistent with $Sm_2Ti_2O_7$ itself having the pyrochlore structure. The principal difference between pyrochlore-type and weberite-type $A_2B_2X_7$ structures is illustrated in Fig. 3. In the different weberite modifications, Fig. 3a and 3b, the BX_6 octahedron in the A_3B layers shares four of its anions with octahedra from the adjacent HTB layers, giving an octahedral framework composition $[B_2X_7]^{n-}$. In pyrochlore, Fig. 3c, the positioning of adjacent A_3B and B_3A layers is such that BX_6 in the B_3A layers share all six vertices with octahedra from the HTB layers on either side. The framework composition is now $[B_2X_6]^{m-}$. The seventh anion is coordinated only to the large A cations, giving an anticristobalite A_2X network of corner-linked A_4X tetrahedra (12).

For pyrochlores of the type $A_2^{2+}B_2^{5+}O_7$, the formal valence sum at the oxygen site in the A_4O tetrahedron is only 1.0. Considerable bond shortening must occur to satisfy the oxygen valence requirements, and so $A_2^{2+}B_2^{5+}O_7$ pyrochlores generally form only with relatively small, electronegative divalent cations such as Cd^{2+}, or when some substitution of F^-, OH^-, H_2O or vacancies occur at the seventh oxygen site or when pressure is applied (13). In 5M $Ca_2Ta_2O_7$, the partial replacement of Ca^{2+} by the smaller, higher valent Sm^{3+} stabilizes the pyrochlore component presumably by satisfying the geometrical matching of the B_2O_6 and A_4O frameworks while meeting the valence requirements of the oxygen in A_4O. The A_4O oxygens in 5M $Ca_2Ta_2O_7$ are O(1) and O(14) in Table 3. The tetrahedral bond lengths of these oxygens to Ca/Sm are all short, with A–O(1) in the 2.16 to 2.31 Å range and A–O(14) in the 2.19 to 2.24 Å range, compared to average A–O distances in the 2.49 to 2.59 Å range.

In 5M $Ca_2Ta_2O_7$, the pyrochlore blocks alternate with weberite blocks as shown in Fig. 5. The weberite blocks have the same interlayer articulation of polyhedra as in 3T weberite, with *cis*-configurations of the octahedra in the large cation layers as shown in Fig. 6. These octahedra, formed by Ta(53), are the most distorted in the structure with Ta(53)–O distances in the 1.90 to 2.17 Å range. The distortion is associated with a relatively large displacement of Ta toward the edge formed by the *cis*-pair of terminal oxygens, resulting in alternating long and short Ta(53)–Ca(5) distances of 3.84 and 3.52 Å in the Ca_3Ta layer at $z = 0.4$. An analogous perturbation was found in the 6T polytype structure as discussed above.

The interface between the pyrochlore and weberite blocks in 5M $Ca_3Ta_2O_7$ is formed by a Ta_3Ca layer which is in hexagonal stacking with the Ca_3Ta layers on either side. Significant differences in coordination result from atom displacements in this part of the structure. Two of the oxygen atoms in the plane of the *h*-stacked cation layer, O(22) and O(23) in Table 3, are only three-coordinated, in contrast to the fluorite-related cubic-stacked blocks where all of the oxygens are four-coordinated. The coordinations

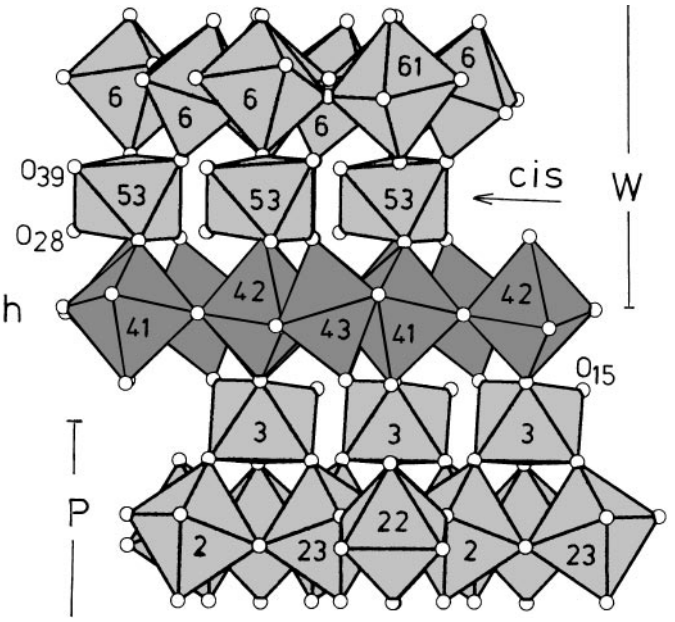

FIG. 6. Part of the 5M octahedral framework rotated 30° about c^* from the projection in Fig. 5. The terminal oxygen atoms associated with TaO_6 in the Ca_3Ta layers are labeled, as are the tantalum atoms, the *h*-stacked layer, and the pyrochlore (P) and weberite (W) blocks.

of the calcium atoms Ca(51) and Ca(52) in the adjacent Ca_3Ta layer of the weberite block are correspondingly modified. Ca(51) has six Ca–O bonds in the 2.29–2.57 Å range, together with three considerably longer distances in the 3.04 to 3.30 Å range. Ca(52) has seven Ca–O bonds in the 2.24 to 2.73 Å range and a longer distance of 3.20 Å.

Within the *h*-stacked Ta_3Ca layer, [010] chains of Ta(42), Ta(43), and Ta(41), Ca(4) are alternately displaced above and below the plane by ~ 0.1 Å, giving a corrugated layer of metals. However, the vertical displacement of the oxygen atoms associated with this plane are smaller than for the other Ta_3Ca planes. This is related to the particular interlayer metal atom distributions due to the pseudo-mirroring across the *h*-stacked layer. In the other Ta_3Ca layers, considerable tilting of the TaO_6 octahedra is required to allow interlayer articulation to the edges of TaO_6 octahedra in the Ca_3Ta layers. However, in the *h*-stacked layer, one of the triangular groupings of corner-linked octahedra has calcium atoms directly above, Ca(51), and below, Ca(31), the triangular cluster. Connection of the apical oxygens of the triangular grouping of TaO_6 octahedra to the much longer polyhedral edges associated with Ca(51) and Ca(31) requires that the tilting of the TaO_6 octahedra is considerably less. This in turn forces the titanium atoms to be displaced from the equatorial plane of oxygens to maintain reasonable bond lengths, causing corrugation of the layers. The largest pertubation to metal atom packing is associated with this particular grouping, whereby Ca(51) is displaced away from

the triangular grouping of Ta(41)–Ta(43), giving a long Ca(51)–Ta(41) distance of 4.07 Å, see Table 6.

GENERAL DISCUSSION

The $Ca_2Ta_2O_7$ structures can be described in various ways to bring out different features. Attention can be focused for exampled on the close-packed array of metal atoms. This brings out the structural relationship between the *c*-stacked tantalate polytypes and other $A_2B_2X_7$ fluorite-derivative structures, including pyrochlore and the weberite and zirconolite polytypes. It also allows the tantalate polytypes such as the 5M, 6M, and 7M phases (1) to be described in terms of twinning of the metal atom array with $\{111\}_f$ as the composition plane for the twinning. The conversion of *c* stacking to *h* stacking of the closest packed layers has analogies with the change from C- to *A*-type Ln_2O_3, Ln = lanthanoid (14), and with the change from cubic to hexagonal ABX_3 perovskites via various mixed *ch* stacking sequences of the closest packed AX_3 layers (15).

In the description based on a close-packed metal atom array the anions are considered to occupy the tetrahedral interstices as in the fluorite structure, and structural systematics can be readily rationalized in terms of the compositions of the cation tetrahedra. For example, the anion vacancies, relative to fluorite M_4X_8, are confined to tetrahedra of composition Ta_3Ca (and Ta_4 in pyrochlore), while the anions in the Ca_3Ta tetrahedra are strongly undersaturated (formal valence = 1.58) and so involve short Ca–O and Ta–O bonds. This can help explain why Ca(51) and Ca(52) in the 5M structure are only seven-coordinated. Both of these calcium atoms have in their coordination sphere three oxygen atoms with Ca_3Ta coordination, and the displacement of the calcium atoms to shortern all three Ca–O distances results in a very long eighth Ca–O distance.

An alternative description of the tantalate polytypes focuses on the framework of TaO_6 corner-linked octahedra. Unlike in pyrochlores, all the oxygen atoms are involved in bonding to the tantalum atoms in the different $Ca_2Ta_2O_7$ polytypes, giving a $[Ta_2O_7]^{4-}$ framework, in which the calcium atoms are distributed in the framework cavities. This description is useful in that it explains an otherwise unusual aspect of the polytype structures. In the known *c*-stacked structures of the 3T and 6T polytypes, as well as the 4M $Na_2Ta_2O_5F_2$ phase (16), pyrochlore and the different weberite polytypes, an invariant structural feature is the relative disposition of the A_3B large-cation layers. The stacking of the A_3B layers is identical in all cases, and the different polytypes are generated solely by the relative location of the B_3A layers. The reason for the invariance of the A_3B stacking is related to the octahedral tilting in the B_3A layers, required for articulation to the octahedra in the A_3B layers, as illustrated in Fig. 3. Because of the cooperative nature of the octahedral tilting in the B_3A layers, the relative positions of the A_3B layers on either side become fixed relative to one another. Any other disposition of A_3B layers other than that observed would place large strains on the interlayer articulation. A related argument has been used to explain the preponderance of particular polymorphs in micas (17). In the case of the mixed-layer $Ca_2Ta_2O_7$ polytypes such as the 5M and 6M structures, the invariance in stacking of the A_3B layers is naturally broken across the *h*-stacked layers, but it is maintained in the *c*-stacked blocks between the *h* planes.

In focusing on the octahedral framework, it is worth noting that the structure of the starting material for preparation of the polytypes, Ta_2O_5, has structural elements in common with the HTB layers in the polytypes. The tantala polymorphs have been described in terms of corner- and edge-linked pentagonal bipyramids and octahedra (18, 19). However, a pentagonal bipyramid sharing two adjacent equatorial edges with octahedra is topologically equivalent to a triangular group of corner-shared octahedra. Thus, only small movements of the seven-coordinated tantalum atoms and associated oxygen atoms are required to convert segments of the Ta_2O_5 structures into regions of HTB structure, and these may well act as nucleating points for the growth of the polytype structures. It is interesting to note that the triangular grouping of corner-linked octahedra is a commonly encountered element in a wide variety of tantalate structures, including hexagonal and tetragonal bronze structures (20), alkali tantalates containing HTB layers directly connected either by corners or edges (21) and structures in which pairs of triangular groupings of tantalate octahedra are connected by edges to form octahedral clusters (20).

A feature of the octahedral framework of the *c*-stacked $Ca_2Ta_2O_7$ phases, in common with all weberite polytypes, is that half of the octahedra have only four vertices involved in the framework connectivity. Thus, in contrast with the rigid framework in pyrochlore in which all vertices of the octahedra are involved in corner sharing, the tantalates have a relatively high degree of structural flexibility to adapt to different types of dopant elements. There are two different types of four-connected octahedra in weberite polytypes. Within the B_3A layers they are always in *trans*- configuration (this is modified in the *h*-stacked Ta_3Ca layers of the 5M $Ca_2Ta_2O_7$, where the four-connected *trans*-TaO_6 is replaced by five-connected octahedra, (see Fig. 6)), whereas within the A_3B layers, the octahedra can have either *cis*- or *trans*- configurations. The *trans*-octahedra act very much like hinges and allow the structure to expand or contract perpendicular to the layers. In the tantalate polytypes for which we have structural data, increasing ratios of *trans*- relative to *cis*-octahedra in the Ca_3Ta layers results in increased rhombic elongation. In contrast to the influence of the *trans*-octahedra on the layer separation, the *cis*-octahedra are associated with large intraplane displacements

and irregular polyhedral coordination. These may play an important role both in providing structural stability via vibrational entropy contributions from the longer ensuing bonds and in determining the dielectric properties of the calcium tantalates.

In systems that exhibit polytypism, the subtle causes that give rise to different polytype sequences are difficult to systematize. The problem is compounded by the non-equilibrium, dynamic nature of the polytype growth processes. In the case of the tantalate polytypes, the role of impurities appears to be important. Doping with $Sm_2Ti_2O_7$ produces polytypes different than those formed in the undoped system, and increasing substitution of $Sm_2Ti_2O_7$ stabilizes a pyrochlore element in the 5M polytype. Increasing substitution of lanthanoids in zirconolite also brings about consistent polytype changes (22) while in the weberite $Na_2M^{3+}M^{2+}F_7$ polytypes a clear correlation has been reported (8) between the size of the divalent cations and the polytype type (percentage of *trans*-octahedral connections). The causes of *h* stacking in the tantalate polytypes are difficult to explain. Such mixed stacking has not been reported for weberite or zirconolite polytypes.

Temperature appears to be important and possibly also small deviations from the 1:1 ratio of large to small cations. We are currently characterizing the structures of a number of new tantalate polytypes, including 3T, 4M, 5M (different to the 5M reported here), and 7M, involving different dopant elements including Nd, Zr, Nb, and Mg with the expectation that the analysis of the larger body of data will help to answer some of the problems raised.

ACKNOWLEDGMENTS

We thank Dennis Minor for help with the preparations, Gary Fallon for assistance with the single crystal data collections, and Ian Harrowfield for carrying out the electron microprobe analyses.

REFERENCES

1. I. E. Grey, R. S. Roth, G. Mumme, L. A. Bendersky, and D. Minor, "Solid State Chemistry of Inorganic Materials II." MRS Special Publication Vol. 547, 127 (1999).
2. K. O'Keefe, "Australasian Mining and Metallurgy," Vol. 2 (J. T. Woodcock and J. K. Hamilton, Eds.), p. 1135, Australasian Institute of Mining and Metallurgy, Melbourne, 1993.
3. H. Aral, J. A. Johnson, and C. Calle, "Chemeca 98, The 26th Australasian Chemical Eng. Conf.," Port Douglas, Quensland, Sept. 1998, paper no. 224 (1998).
4. R. J. Cava, J. J. Krajewski, and R. S. Roth, *Mater. Res. Bull.* **33,** 527 (1998).
5. J. T. Lewandowski, I. J. Pickering, and A. J. Jacobson, *Mater. Res. Bull.* **27,** 981 (1992).
6. P. P. Leshchenko, O. N. Kalinina, L. N. Lykova, and L. M. Kovba, *Neorg. Mater.* **18**(2), 333 (1982).
7. W. Verscharen and D. Babel, *J. Solid State Chem.* **24,** 405 (1978).
8. G. Yakubovich, V. Urusov, W. Massa, G. Frenzen, and D. Babel, *Z. Anorg. Allg. Chem.* **619,** 1909 (1993).
9. G. M. Sheldrick, "SHELX93, Program for the Refinement of Crystal Structures." Univ. Gottingen, 1993.
10. R. D. Shannon, *Acta Crystallogr. Sect. A* **32,** 751 (1976).
11. N. E. Brese and M. O'Keeffe, *Acta Crystallogr. Sect. B* **47,** 192 (1991).
12. J. Pannetier and J. Lucas, *Mater. Res. Bull.* **5,** 797 (1970).
13. M. A. Subramanian, G. Aravamudan, and G. V. Subba Rao, *Prog. Solid. State Chem.* **15,** 55 (1983).
14. P. E. Caro, *J. Less-Common Met.* **16,** 367 (1968).
15. J. B. Goodenough and J. M. Longo, *in* "Landolt–Bornstein—Numerical Data and Functional Relationships in Science and Technology" (K.-H. Hellwege and A. M. Hellwege, Eds.), Group III, Vol. 4a, p. 126. Springer-Verlag, Berlin, 1970.
16. M. Vlasse, J. P. Chaminade, J. C. Massies, and M. Pouchard, *J. Solid State Chem.* **12,** 102 (1975).
17. E. W. Radoslovich, *Nature* 4656, 253 (1959).
18. N. C. Stephenson and R. S. Roth, *Acta Crystallogr. Sect. B* **27,** 1037 (1971).
19. N. C. Stephenson and R. S. Roth, *J. Solid State Chem.* **3,** 145 (1971).
20. B. M. Gatehouse, *J. Less-Common Met.* **50,** 139 (1976).
21. K. Yagi and R. S. Roth, *Acta Crystallogr. Sect. A* **34,** 765 (1978).
22. K. L. Smith and G. R. Lumpkin, "Defects and Processes in the Solid State: Geoscience Applications" (J. N. Boland and J. D. Fitzgerald, Eds.), The McLaren Volume, p. 401. Elsevier, Amsterdam, 1993.